CHINA FOUNDRY Research & Development
Vol.19 No.2 March 2022
www.springer.com/41230
https://doi.org/10.1007/s41230-022-1066-6

Effect of processing parameters on formability, microstructure, and micro-hardness of a novel laser additive manufactured Ti-6.38Al-3.87V-2.43Mo alloy

Tian-yu Liu[1], Zhi-hao Zhu[1], Shuang Zhang[2], **Xiao-hua Min[1], and *Chuang Dong[1, 2]

1. School of Materials Science and Engineering, Dalian University of Technology, Dalian 116024, Liaoning, China
2. School of Materials Science and Engineering, Dalian Jiaotong University, Dalian 116028, Liaoning, China

Abstract: A novel Ti-6.38Al-3.87V-2.43Mo alloy was designed with a cluster formula of 12[Al-Ti_{12}]($V_{0.75}Mo_{0.25}Ti_2$)+4[Al-Ti_{12}](Al_3) by replacing Ti with Mo/V on the basis of the Ti-Al congruent alloy. The effects of laser power and scanning speed on the molten pool size, surface roughness, relative density, microstructure, and micro-hardness of single-track and bulk Ti-6.38Al-3.87V-2.43Mo samples prepared via laser additive manufacturing (LAM) were investigated. The results show that processing parameters significantly affect the formability, microstructure, and micro-hardness of the alloy. With decreasing laser power from 1,900 W to 1,000 W, the relative density is decreased from 99.86% to 90.91% due to the increase of lack-of-fusion; however, with increasing scanning speed, the relative density does not change significantly, but exceeds 99%. In particular, Ti-6.38Al-3.87V-2.43Mo samples of single-track and bulk exhibit a good formability under an input laser power of 1,900 W and a scanning speed of 8 $mm\cdot s^{-1}$, and display the lowest surface roughness (Ra=13.33 μm) and the highest relative density (99.86%). Besides, the microstructure of LAM Ti-6.38Al-3.87V-2.43Mo alloy coarsens with increasing laser power or decreasing scanning speed due to the greater input energy reducing the cooling rate. The coarsening of the microstructure decreases the microhardness of the alloy.

Keywords: laser additive manufacturing; composition design; cluster-plus-glue-atom model; microstructure; properties

CLC numbers: TG146.23 **Document code:** A **Article ID:** 1672-6421(2022)02-158-11

1 Introduction

Titanium alloys have been applied widely in chemistry, aerospace, shipbuilding, and other industrial applications because of their excellent properties, such as a high strength-to-weight ratio, low density, excellent corrosion resistance and fracture roughness [1-3]. However, large and complex titanium alloy components manufactured via conventional processing technologies are still facing great challenges. In recent years, laser additive manufacturing (LAM) of 3D parts via an incremental layer-by-layer method directly [4] has attracted wide attention. However, only a few titanium alloys are suitable for LAM [5, 6], hindering the development of LAM.

The binary TiAl phase diagram shown in Fig. 1 indicates that the special composition of Ti-11at.%Al lies at the coincidence of liquidus and solidus. The congruent alloy behaves like a pure metal as it melts and freezes isothermally, indicating that it has excellent composition uniformity [7, 8]. Therefore, Ti-11at.% Al alloy is suitable for use in LAM. However, the low strength of this binary alloy limits its application, so it is necessary to add alloying elements to further improve its strength.

A cluster-plus-glue-atom (CPGA) model was proposed by Dong et al. [9-11] to deal with the chemical short-range order (SRO). In this model, the characteristic SRO structure is simplified into a local structural unit, in which the interaction between atoms is best satisfied locally, covering only the nearest neighbors and a few outer-shell atoms. The unit then adopts a [cluster](glue atoms)$_x$ formula, indicating that one cluster is matched with a few glue atoms [12]. Such

***Chuang Dong**
Male, Ph. D, Professor. His research interests mainly focus on structural modeling of disordered materials, alloy design, and surface modification. Prof. Dong owned the title of the Outstanding Young Researcher in 1995 and Changjiang Professor in 2005, respectively.
E-mail: dong@dlut.edu.cn

****Xiao-hua Min**
E-mail: minxiaohua@dlut.edu.cn

Received: 2021-04-01; Accepted: 2021-12-13

a CPGA model can be used to develop the multicomponent alloys that exhibit high performance [13-15].

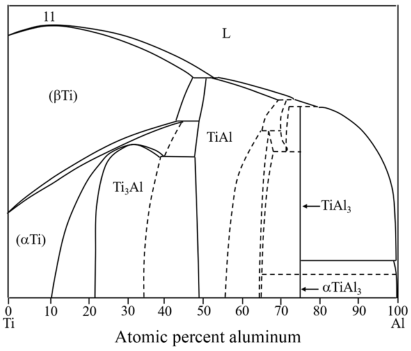

Fig. 1: Ti-Al binary phase diagram

Further, the formability, microstructure, and mechanical properties of LAM titanium alloy parts are significantly affected by the processing parameters, especially by laser power and scanning speed [16]. Yang et al. [17] found a better combination of strength and ductility with increasing laser power or decreasing scanning speed. Furthermore, work by Thijis et al. [18] suggested that the porosity of LAM titanium alloys was related to the variation in the energy density of the process. In this situation, the combination of optimizing chemical composition and LAM processing parameters is an effective way to develop high-performance titanium alloys.

From this, a Ti-6.38Al-3.87V-2.43Mo alloy with a cluster formula of $\mathrm{12[Al\text{-}Ti_{12}](V_{0.75}Mo_{0.25}Ti_2)+4[Al\text{-}Ti_{12}](Al_3)}$ was designed by replacing Ti with Mo/V on the basis of the Ti-Al congruent alloy. The effects of laser power and scanning speed on the molten pool size, surface roughness, relative density, microstructure, and micro-hardness of single-track and bulk Ti-6.38Al-3.87V-2.43Mo samples prepared via LAM were investigated.

2 Materials and methods

2.1 Composition design

Many researchers [19, 20] have investigated the SRO of congruent alloys, and they have found that the SRO parameter α_i had a significant difference at both sides of the congruent point, indicating that a congruent alloy contains two subunits which originate from two relative phases. Thus, a dual-cluster model was proposed to interpret the congruent alloy. At the Ti-11at.% Al congruent point, as shown in Fig. 1, the relevant phases are α-Ti (hexagonal close-packed structure) and $\mathrm{Ti_3Al}$ phase ($\mathrm{Ni_3Sn}$ structure type, space group P4/mmm, where the crystal structure data are taken from Pearson's handbook) [21]. The α-Ti solid solution contains a $\mathrm{[Al\text{-}Ti_{12}]}$ cluster because of the strong interactions between Al and Ti [22]. In the $\mathrm{Ti_3Al}$ phase, there are two types of clusters, $\mathrm{[Al\text{-}Ti_{12}]}$ and $\mathrm{[Ti\text{-}Al_4Ti_8]}$, with two nonequivalent atomic sites at their centers. Of these, $\mathrm{[Al\text{-}Ti_{12}]}$ should be considered as the principal cluster following the criteria proposed in the study [23], which describes the principal cluster as exhibiting interatomic force constants higher than the other clusters. The dual-cluster formula is: $\mathrm{Ti_{89}Al_{11} \rightarrow 12[Al\text{-}Ti_{12}](Ti_3)+4[Al\text{-}Ti_{12}](Al_3)=Al_{28}Ti_{228}=Al_{10.94}Ti_{89.86}}$ (at.%), where 12:4 (3:1) satisfies the homogeneous solute distribution model [24].

It has been proven that the hardening effect of the four isomorphous β stable elements decreases systematically in the order of Mo>V>Nb>Ta [25]. Besides this, the solute elements Mo and V, which form weak interactions with Ti, occupy the cluster glue atom positions [4]. Thus, the Ti-6.38Al-3.87V-2.43Mo alloy with a cluster composition formula of $\mathrm{12[Al\text{-}Ti_{12}](V_{0.75}Mo_{0.25}Ti)+4[Al\text{-}Ti_{12}](Al_3)}$ was designed by replacing Ti with Mo/V on the basis of the Ti-Al congruent alloy.

Ti and Al powder particles with a size range of 50–150 μm, and V and Mo powder particles with a size range of 50–75 μm were used to prepare a Ti-6.38Al-3.87V-2.43Mo alloy sample. The elemental powder particles were firstly proportionally mixed based on the desired compositions, and subsequently dried for 12 h in a vacuum drying furnace at 120 °C, followed by mixing in a blending machine for 8 h. Figure 2 shows the mixed powder morphology and the elemental distribution of Ti-6.38Al-3.87V-2.43Mo, indicating that the alloying elements of Al, V and Mo are uniformly distributed. The melting point of the novel alloy was 1,948 K, as calculated using JMatPro software.

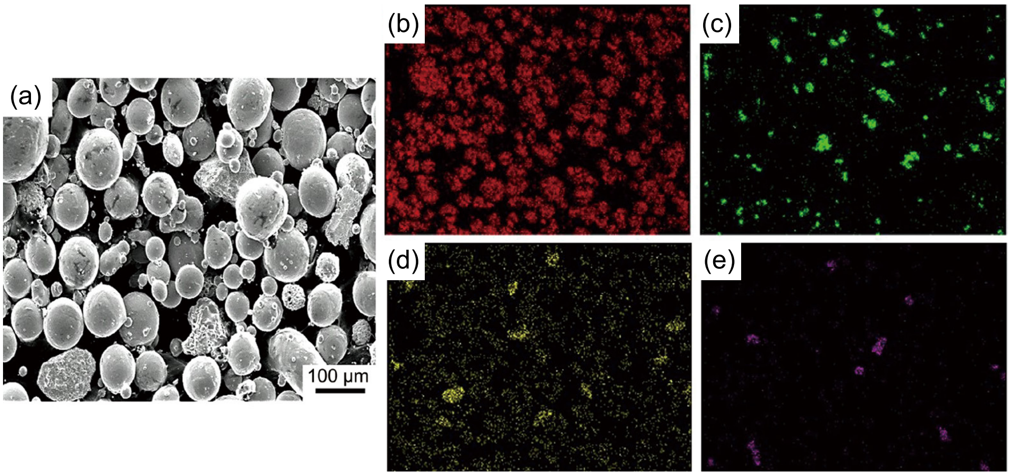

Fig. 2: Mixed powder morphology (a) and its elemental distribution (b–e) of Ti-6.38Al-3.87V-2.43Mo alloy: (b) Ti element; (c) Al element; (d) V element; (e) Mo element

2.2 Laser additive manufacturing

Samples were deposited via the LAM system which involved a 6-kW fiber laser, a four-nozzle coaxial powder feed system, a controlled environment glove box, and a motion control system [3, 4]. The single-track samples were performed at a scanning speed of 8 mm·s^{-1} and laser powers of 1,000 W, 1,300 W, 1,600 W, 1,900 W, 2,200 W and 2,500 W; and at a laser power of 1,900 W and scanning speeds of 4 mm·s^{-1}, 6 mm·s^{-1}, 8 mm·s^{-1}, 10 mm·s^{-1}, 12 mm·s^{-1}, and 14 mm·s^{-1}, respectively. The bulk samples were performed at a scanning speed of 8 mm·s^{-1} and laser powers of 700 W, 1,000 W, 1,300 W, 1,600 W and 1,900 W, and at a laser power of 1,900 W and scanning speeds of 6 mm·s^{-1}, 8 mm·s^{-1}, 10 mm·s^{-1}, 12 mm·s^{-1}, and 14 mm·s^{-1}, respectively. All processes were carried out under the protective atmosphere of pure argon during the fabrication process. To achieve the continuous deposition of layers, the overlapping fraction of the parallel tracks portion was 30%. During the multilayer deposition process, the layer thickness in the *Z* direction was set as 0.6 mm, and a zigzag-pattern-scanning strategy was used, as shown in Fig. 3. The substrate used was a Ti-6Al-4V plate with dimensions of 60 mm×60 mm×15 mm. Furthermore, EPMA analysis was conducted to determine the distribution of alloy elements of a sample prepared using a laser power of 1,900 W at a scanning speed of 8 mm·s^{-1}, as shown in Fig. 4, from which it is verified that the alloy elements are distributed uniformly.

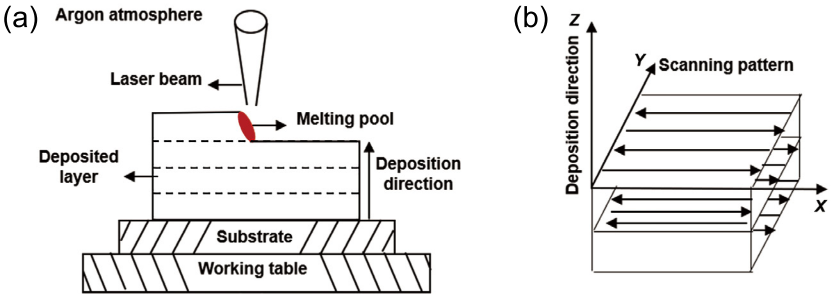

Fig. 3: Schematic diagram of LAM processing method (a) and strategy used to scan bulk samples (b)

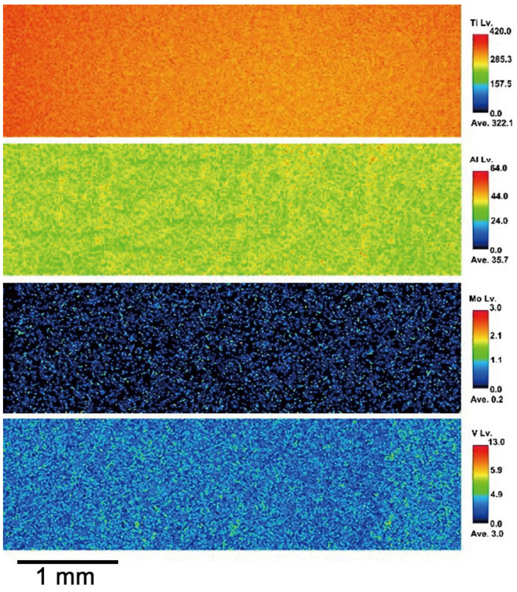

Fig. 4: EPMA elemental distribution of Ti-6.38Al-3.87V-2.43Mo alloy developed by a laser power of 1,900 W at a scanning speed of 8 mm·s^{-1}

2.3 Microstructures and properties

The representative microstructures of the single-track and bulk LAM samples on the longitudinal section were observed via an Olympus optical microscope and a Zeiss Supra55 scanning electron microscope. The molten pool sizes of the single-track samples were acquired by an averaging of three single-track samples at three different positions. The relative density of the bulk samples was attained via an XS64 densimeter. In addition, phases present in the bulk samples were detected via a D8 focus X-ray diffractometer equipped with a Cu Kα radiation source, operating at 40 kV and 40 mA and at a scanning rate of 4°·min^{-1} over an angle range of 20°–100°. Micro-hardness testing of the LAM bulk samples was carried out on HVS-1000 apparatus with a load of 300 g for 15 s.

3 Results

3.1 Influence of processing parameters on single-track samples

3.1.1 Effect of laser power on single-track samples

Figures 5 and 6 respectively show the macro- and micro-structures of the molten pools at different laser powers with a constant scanning speed of 8 mm·s^{-1}. It can be seen from Fig. 5(a) at a laser power of 1,000 W, pores are formed between the single-track samples and the substrate because of lower incident energy. When a single-track was deposited on the substrate with laser power 1,900 W to 2,500 W, the substrate is partially remelted, leading to a good fusion between the single-track samples and the substrate, as shown in Figs. 5(d–f). Besides this, the formation of β columnar grains of LAM Ti-6.38Al-3.87V-2.43Mo alloy along the deposition direction can be observed in Figs. 5(a–f). With an increase in the laser power, the width of β columnar grains increases from 99.37 to 181.11 µm, as shown in Fig. 5(g). Figure 6 shows the microstructure within the β columnar grains, in which the lamellae α and acicular α' phases can be observed. Clearly, the acicular α' phase is thinner than the lamellae α. It is evident that the microstructure consists mainly of acicular α' phases at a low laser power, as shown in Figs. 6(a) and (b). In contrast, the microstructure contains mainly lamellae α phases when the laser power is high, as shown in Figs. 6(c–f).

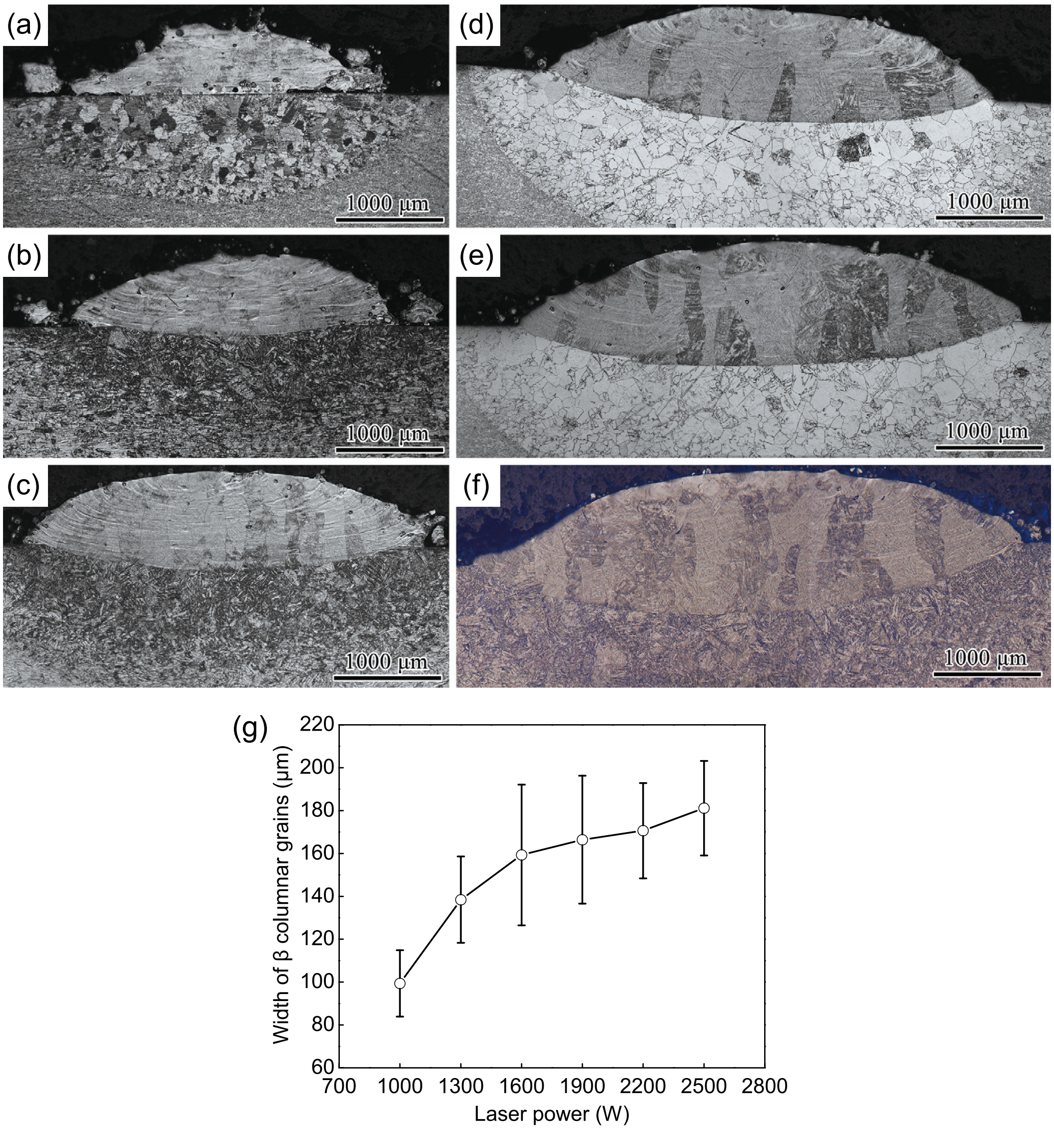

Fig. 5: Cross sections of molten pools under different laser powers *P* with a constant scanning speed of 8 mm·s^{-1}: (a) *P*=1,000 W; (b) *P*=1,300 W; (c) *P*=1,600 W; (d) *P*=1,900 W; (e) *P*=2,200 W; (f) *P*=2,500 W; and changes in widths of β columnar grains (g)

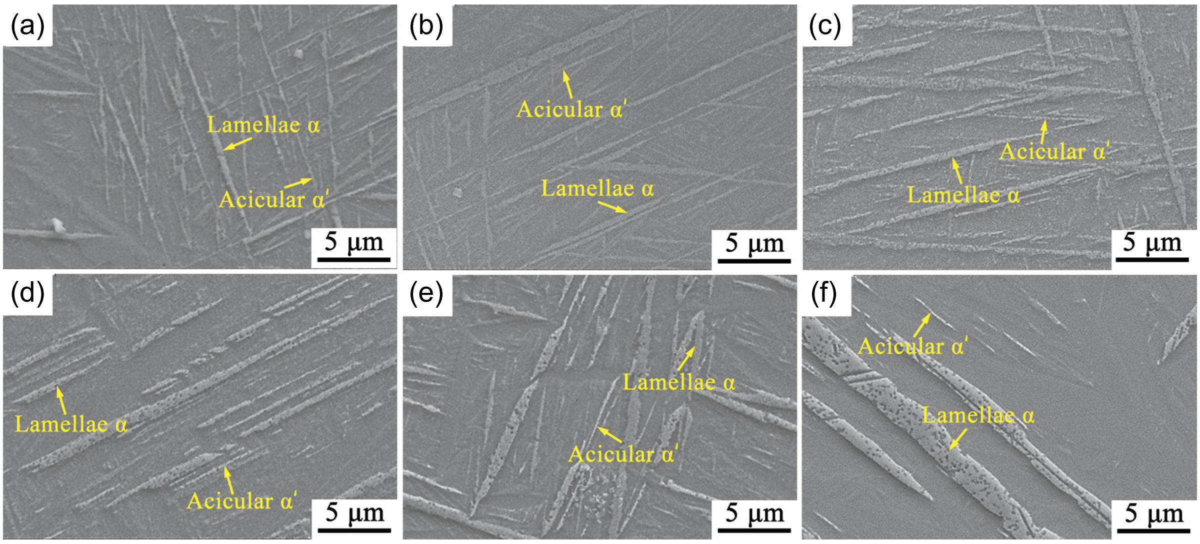

Fig. 6: Microstructures of designed alloy produced at different laser powers of *P*=1,000 W (a), *P*=1,300 W (b), *P*=1,600 W (c), *P*=1,900 W (d), *P*=2,200 W (e), and *P*= 2,500 W (f), with a constant scanning speed of 8 mm·s^{-1}

As LAM is a layer-by-layer built process, the height, width, and depth of the molten pool determine the metallurgical bonding capacity between adjacent layers. So, the changes in the molten pool size at different laser powers were measured, with results shown in Fig. 7(a). Clearly, with an increase in the laser power, there is a distinct upward trend in the depth (0–0.55 mm). The trend of the change in the width and height can be divided into two stages: when the laser power is lower than 1,900 W, the upward trend is more obvious, whereas when the laser power is higher than 1,900 W, the uptrend gradually slows down. Furthermore, Fig. 7(b) displays the depth-to-width and height-to-width ratio of molten pools. A sharp upward trend of depth-to-width ratio is observed with increasing the laser power from 1,000 W to 1,600 W; conversely, the height-to-width ratio visibly reduces. When the laser power is increased from 1,600 W to 2,200 W, the depth-to-width and height-to-width ratio vary slow down. It is determined that the optimal laser power is 1,900 W for the single-track alloy according to Figs. 5 and 7.

The results of surface roughness at different laser powers are shown in Fig. 8. The adhesion of partially unmelted powder on the single-track sample plays an important role in deteriorating its surface quality. The highest surface roughness (*Ra*=28.30 μm) is obtained at a laser power of 1,000 W. As the laser power increases to 1,900 W, the surface roughness decreases to 13.33 μm. However, the surface roughness increases to 17.18 μm due to the occurrence of powder evaporation under a high laser power of 2,500 W. Generally, a higher surface roughness leads to an increased porosity.

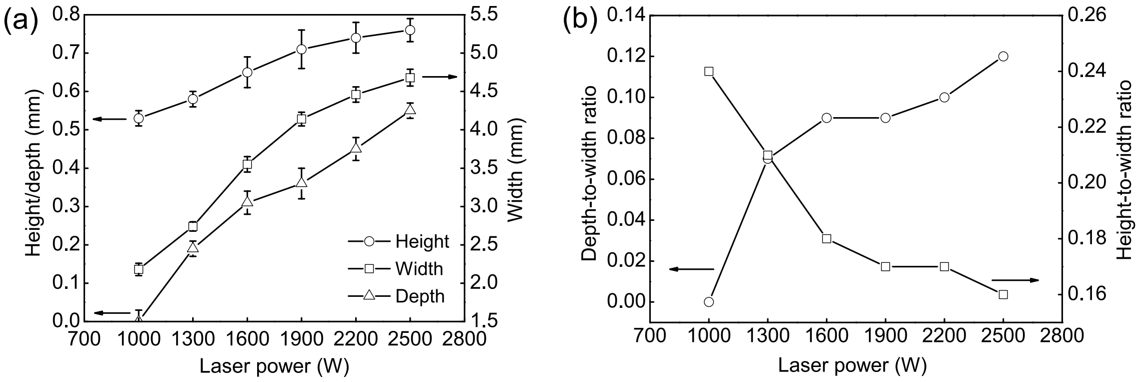

Fig. 7: Changes in molten pool size (a) and depth-to-width and height-to-width ratio of molten pools (b) at different laser powers with a constant scanning speed of 8 mm·s^{-1}

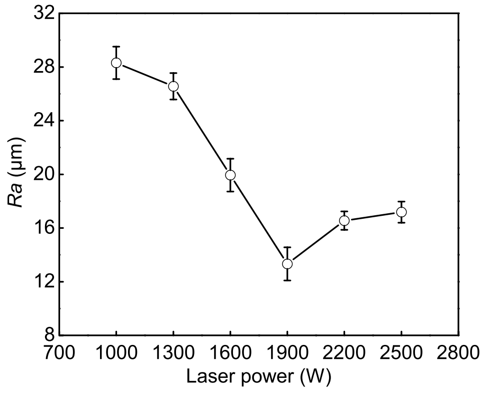

Fig. 8: Changes in surface roughness at different laser powers with a constant scanning speed of 8 mm·s^{-1}

3.1.2 Effect of scanning speed on single-track samples

Figures 9 and 10 respectively show the macro- and micro-structures of the molten pools at different scanning speeds with a constant laser power of 1,900 W. The results show a good fusion between the single-track samples and the substrate with the scanning speeds increase from 4 mm·s^{-1} to 14 mm·s^{-1}. The microstructures are similar to the images shown in Figs. 5 and 6, which show β columnar grains, and the lamellae α and acicular α' phases. The width of the β columnar grains decreases from 186.30 to 117.56 μm with the increase of scanning speed, as shown in Fig. 9(g).

Figure 11 shows the molten pool size of cross sections of the single-track samples at different scanning speeds. As can be seen, the height, width, and depth of the molten pool all decrease with the increase of scanning speed, with changes in the height from 1.30 to 0.39 mm, width from 5.34 to 3.54 mm, and depth from 0.59 to 0.36 mm. Furthermore, Fig. 11(b) exhibits the depth-to-width ratio and height-to-width ratio of molten pools. A sharp downward trend of depth-to-width ratio and height-to-width ratio is found when the scanning speed is increased from 4 mm·s^{-1} to 8 mm·s^{-1}, and then it is bascially unchanged when the scanning speed is increased from 8 mm·s^{-1} to 10 mm·s^{-1}. Combined with Figs. 9(a–f), a good metallurgical bonding capacity is realized when the scanning speed is under 8 mm·s^{-1}, indications are that the optimal scanning speed is 8 mm·s^{-1} for the single-track alloy.

Figure 12 shows the surface roughness of the single-track samples at different scanning speeds. Increasing the scanning speed from 4 mm·s^{-1} to 8 mm·s^{-1}, the surface roughness decreases from 30.74 μm to 13.33 μm. In contrast, as the scanning speed continues to increase to 14 mm·s^{-1}, the surface roughness increases to 26.76 μm. This is because, at a constant laser power of 1,900 W, when the scanning speed is low, the laser energy density is higher and the liquid may be sputtering in the molten pool, which gives rise to a higher surface roughness. When the scanning speed is over 8 mm·s^{-1}, the powders cannot be completely melted because of the low energy density input, resulting in the increase of surface roughness. As mentioned above, the surface roughness and formability of single-track samples are significantly improved via optimizing the laser power being 1,900 W and scanning speed being 8 mm·s^{-1}. To optimize LAM processing parameters for bulk samples, the analysis of processing parameters for single-track samples is conducted as useful guidance for narrowing the parameter range.

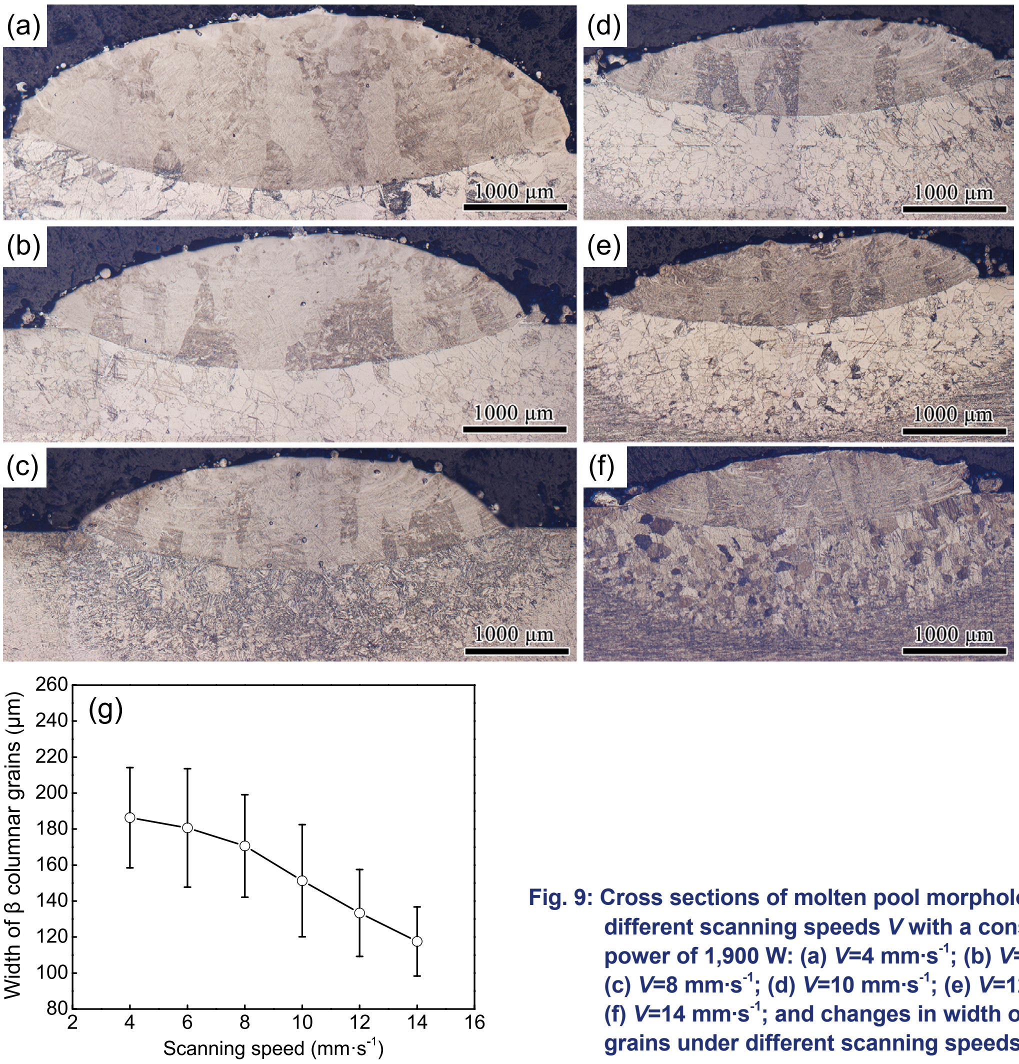

Fig. 9: Cross sections of molten pool morphologies under different scanning speeds *V* with a constant laser power of 1,900 W: (a) *V*=4 mm·s^{-1}; (b) *V*=6 mm·s^{-1}; (c) *V*=8 mm·s^{-1}; (d) *V*=10 mm·s^{-1}; (e) *V*=12 mm·s^{-1}; (f) *V*=14 mm·s^{-1}; and changes in width of β columnar grains under different scanning speeds (g)

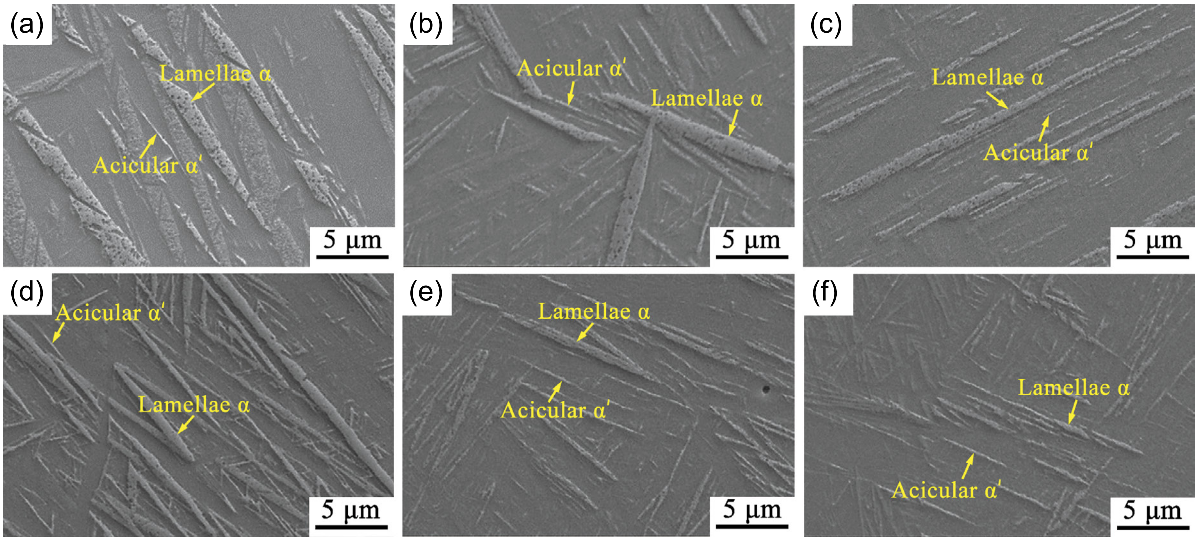

Fig. 10: Microstructures of sample produced at different scanning speeds *V* with a constant laser power of 1,900 W: (a) *V*=4 mm·s^{-1}; (b) *V*=6 mm·s^{-1}; (c) *V*=8 mm·s^{-1}; (d) *V*=10 mm·s^{-1}; (e) *V*=12 mm·s^{-1}; (f) *V*=14 mm·s^{-1}

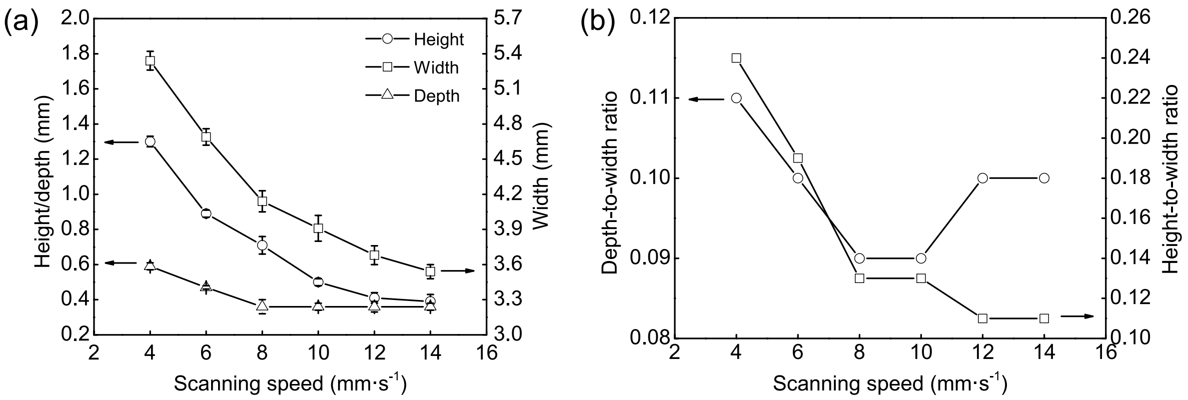

Fig. 11: Changes in molten pool size (a) and depth-to-width ratio and height-to-width ratio of molten pools (b) at different scanning speeds with a constant laser power of 1,900 W

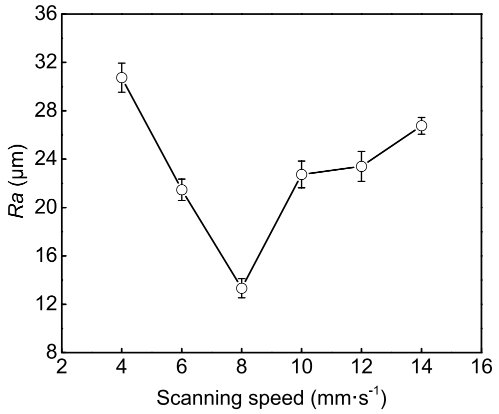

Fig. 12: Changes in surface roughness at different scanning speeds with a constant laser power of 1,900 W

3.2 Influence of processing parameters on bulk samples

3.2.1 Influence of processing parameters on relative density

Figure 13 shows the changes on relative density at different laser powers and scanning speeds. As can be seen from Fig. 13(a), at a laser power of 700 W, the relative density is only 90.91%. The relative density gradually increases with the increase of the laser power. At a laser power of 1,900 W, the relative density is the highest, reaching 99.86%. As Fig. 13(b) shows, the relative density decreases gradually with an increase in the scanning speed, whereas the decrease is small and the density is all over 99%, indicating that the scanning speed has less influence on the density than the laser power.

3.2.2 Effect of laser power on bulk samples

Figure 14 shows the influence of laser power on the macrostructure of Ti-6.38Al-3.87V-2.43Mo bulk samples. With the increase of the laser power from 700 to 1,300 W, the lack-of-fusion is observed in the bulk samples [Figs. 14(a–c)]. When laser powers increase from 1,600 and 1,900 W [Figs. 14(d, e)], there is no lack-of-fusion. Furthermore, the microstructure mainly contains prior-β columnar grains of different lengths at different laser powers. When the laser power is low, as shown in Figs. 14(a–c), the epitaxial growth tendency of the prior-β columnar grains is weaker which contributes to the deposition layer inability to form a good metallurgical bond, reducing the lengths of prior-β columnar grains. With an increase of laser power from 1,600 to 1,900 W, the prior-β columnar grains continue to an epitaxial growth which exceeds multiple deposition layers, as shown in Figs. 14(d, e).

Figures 15 and 16 show the changes in the α grains of the cross sections of the bulk samples at different laser powers. With an increase in the laser power from 700 to 1,900 W, the width of the α laths increases from 0.10 to 0.18 μm. There is a difference in size of α laths for bulk samples and their corresponding single-track ones, which is caused by the bulk samples produced by the incremental layer-by-layer method, and the generated heat can affect adjacent tissues.

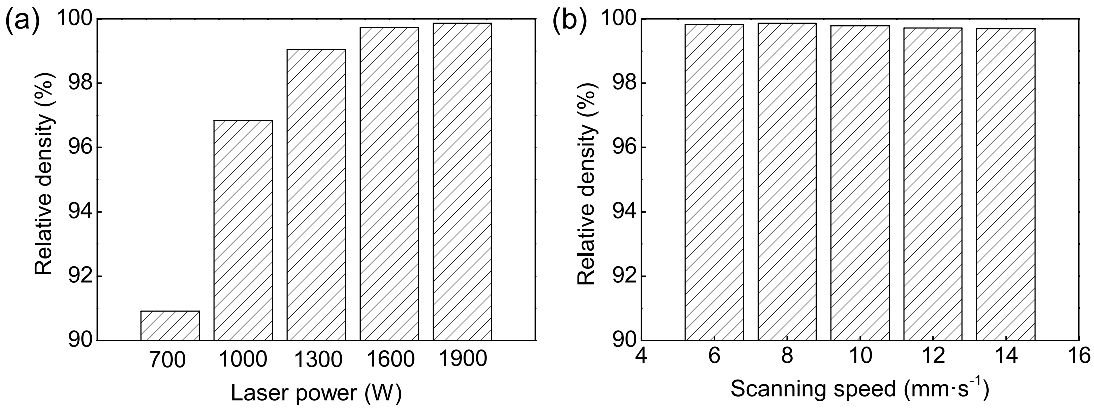

Fig. 13: Effects of laser power (a constant scanning speed of 8 mm·s^{-1}) (a) and scanning speed (a constant laser power of 1,900 W) (b) on relative density

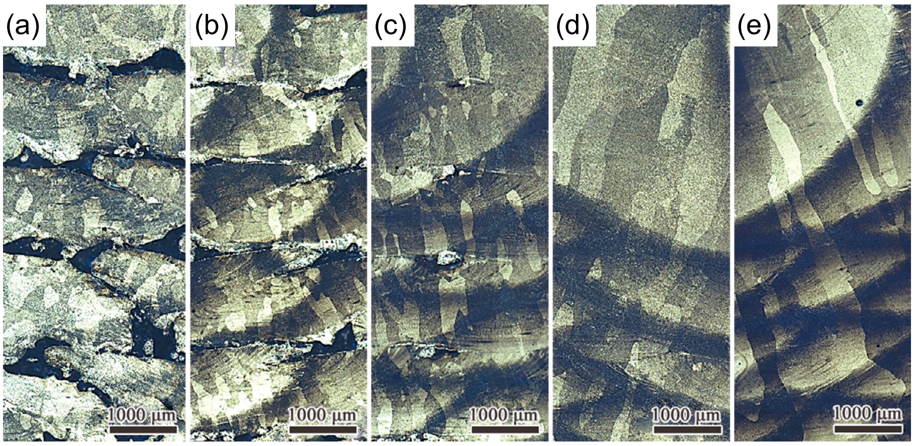

Fig. 14: Change in macrostructures of bulk samples at different laser powers *P* with a constant scanning speed of 8 mm·s^{-1}: (a) *P*=700 W; (b) *P*=1,000 W; (c) *P*=1,300 W; (d) *P*=1,600 W; (e) *P*=1,900 W

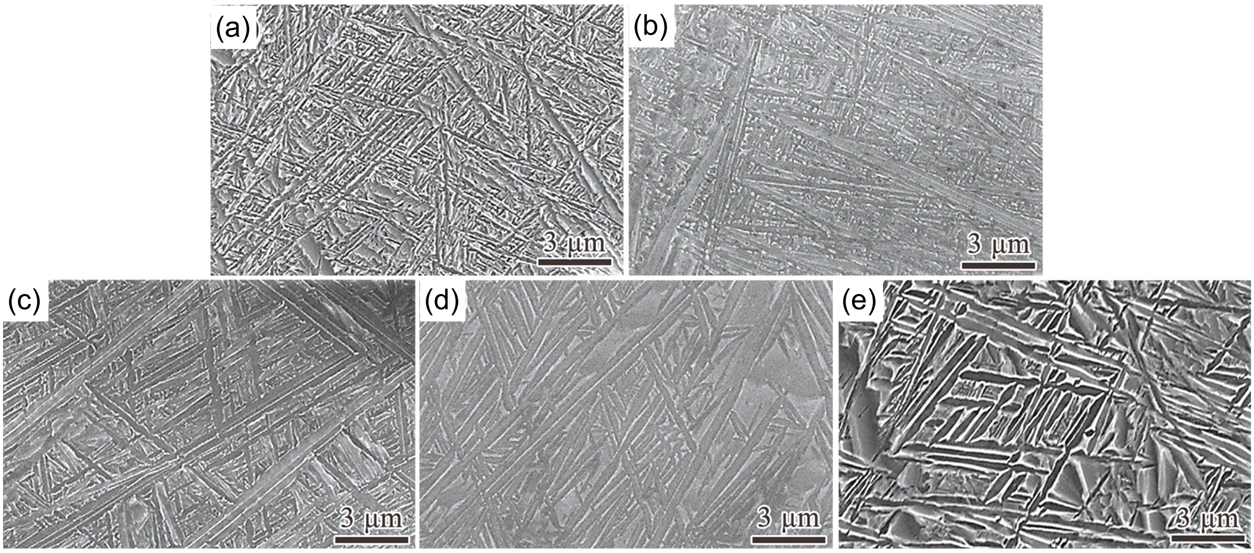

Fig. 15: Change in α grains of cross sections of bulk samples at different laser powers *P* with a constant scanning speed of 8 mm·s^{-1}: (a) *P*=700 W; (b) *P*=1,000 W; (c) *P*=1,300 W; (d) *P*=1,600 W; (e) *P*=1,900 W

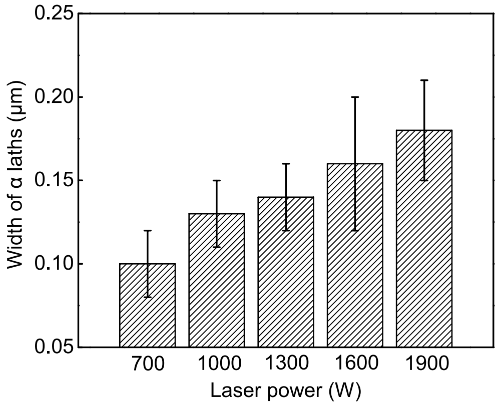

Fig. 16: Changes in width of α laths at different laser powers with a constant scanning speed of 8 mm·s^{-1}

Figure 17 shows the X-ray diffraction (XRD) patterns of the cross sections of the bulk samples at different laser powers. It is evident that the microstructure of the Ti-6.38Al-3.87V-2.43Mo alloy exhibits an α+β dual phase. Figure 18 displays the changes in micro-hardness of cross sections of bulk samples under different laser powers. From these results, it is observed that with increasing laser power from 1,000 W to 1,900 W, the micro-hardness decreases from 402 to 340 HV. Particularly, at a laser power of 700 W, the micro-hardness is only 338 HV.

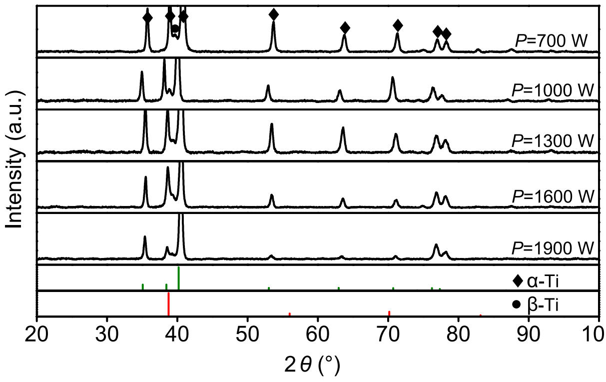

Fig. 17: XRD patterns of cross sections of bulk samples at different laser powers with a constant scanning speed of 8 mm·s^{-1}

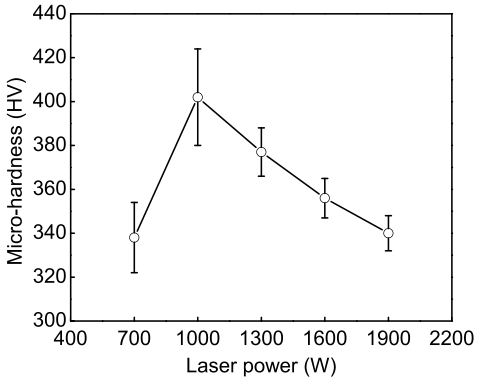

Fig. 18: Changes in micro-hardness of cross sections of bulk samples under different laser powers with a constant scanning speed of 8 mm·s^{-1}

3.2.3 Effect of scanning speed on bulk samples

Figure 19 shows the influence of the scanning speed on the macrostructure of the Ti-6.38Al-3.87V-2.43Mo bulk samples. As can be seen in Fig. 19, at a laser power of 1,900 W, there is no apparent lack-of-fusion defects in all alloys at different scanning speeds. Besides this, with the increasing scanning speed, the height of the bulk samples apparently decreases when depositing the same deposited layers, which is related to the deposition of powder, and a faster scanning speed decreases the deposition of the powder so as to reduce the height of the samples.

Figures 20 and 21 show the changes in the α laths on the cross sections of the bulk samples at different scanning speeds. With the increasing scanning speed, the microstructure features change gradually from a basket-weave structure to a Widmanstätten structure, and the width of the α laths decreases from 0.27 to 0.13 µm.

Figure 22 shows the XRD patterns of the cross sections of the bulk samples at different scanning speeds. Only in the 6 mm·s^{-1} sample exhibits an α+β dual phase. Figure 23 exhibits the changes in micro-hardness of cross sections of bulk samples at different scanning speeds. The micro-hardness gradually increases from 330 to 382 HV with increasing scanning speed.

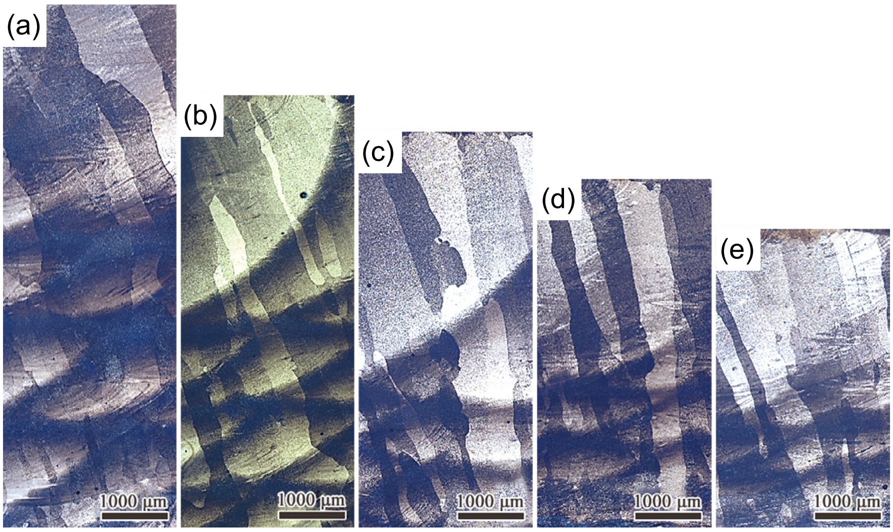

Fig. 19: Changes in macrostructure of bulk samples at different scanning speeds *V* with a constant laser power of 1,900 W: (a) *V*=6 mm·s^{-1}; (b) *V*=8 mm·s^{-1}; (c) *V*=10 mm·s^{-1}; (d) *V*=12 mm·s^{-1}; (e) *V*=14 mm·s^{-1}

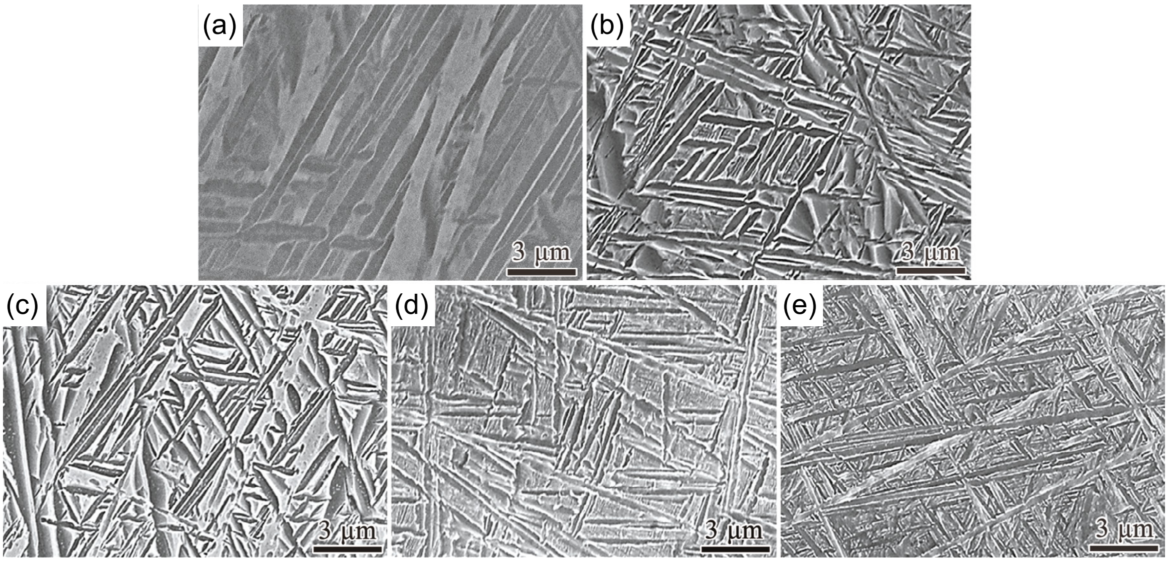

Fig. 20: Changes in α grains on cross sections of bulk samples at different scanning speeds *V* with a constant laser power of 1,900 W: (a) *V*=6 mm·s^{-1}; (b) *V*=8 mm·s^{-1}; (c) *V*=10 mm·s^{-1}; (d) *V*=12 mm·s^{-1}; (e) *V*=14 mm·s^{-1}

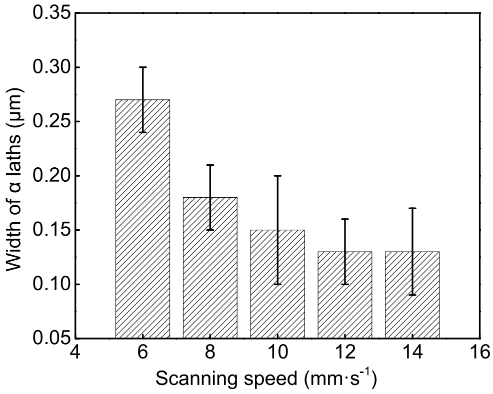

Fig. 21: Changes in width of α laths at different scanning speeds with a constant laser power of 1,900 W

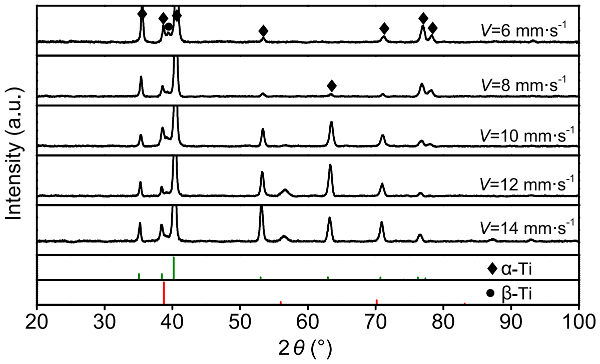

Fig. 22: XRD patterns of cross sections of bulk samples at different scanning speeds with a constant laser power of 1,900 W

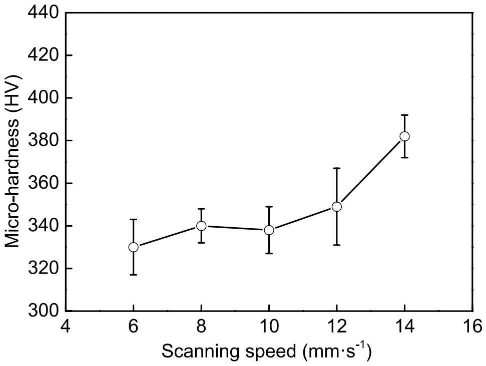

Fig. 23: Changes in micro-hardness of cross sections of bulk samples at different scanning speeds with a constant laser power of 1,900 W

4 Discussion

During the LAM process, the input energy can be evaluated from the volumetric energy density (E_v, in J·mm^{-3}), which can be expressed as follows[26]:

$$E_v = P/Vht \tag{1}$$

where P is the laser power (W), V is the scanning speed (mm·s^{-1}), h is the hatch spacing (mm), and t is the layer thickness (mm). As increasing the laser power or decreasing the scanning speed, the increasing energy input into the molten pool reduces the cooling rate. Therefore, with increasing laser power or decreasing the scanning speed, the width of α laths increases, as shown in Figs. 16 and 21, and the content of β phase decreases, as shown in Figs. 17 and 22.

The maximum temperature (T_{max}) of the laser beam can be calculated using the following equation[27]:

$$T_{max} = \frac{\sqrt{2}AId}{k\sqrt{\pi}}\tan^{-1}\frac{\sqrt{2Dt}}{d} \tag{2}$$

where A is the absorption coefficient, I is the laser intensity, k is the thermal conductivity, D is the thermal diffusivity, t is the interaction time between the laser beam and metal powders, and d is the diameter of the laser beam. Furthermore, t can be calculated from scanning speed V:

$$t = \frac{d}{V} \tag{3}$$

The laser beam size, d, is 2.5×10^{-3} m, the thermophysical parameters of the Ti alloy are A=0.70, k=21 W·m^{-1}·K^{-1}, and D=1.07×10^{-9} m^2·s^{-1}, according to the works of Mills and Rubenchik[28, 29], respectively.

Figure 24 shows the changes in the peak temperature of the molten pool under different process parameters. The data show that the peak temperature of the molten pool (T_{max}) increases from 815 to 2,910 K in line with an increase in the laser power from 700 to 2,500 W with a constant scanning speed of 8 mm·s^{-1}, whereas it decreases from 3,406 to 1,768 K with an increase in the scanning speed from 4 to 14 mm·s^{-1} with a constant laser power of 1,900 W. When the power density of the laser beam is extremely high, the metallic material evaporates. The evaporation of the powder results in the development of a vapor cavity and increases the surface roughness. However, the powder does not melt completely at a low energy density.

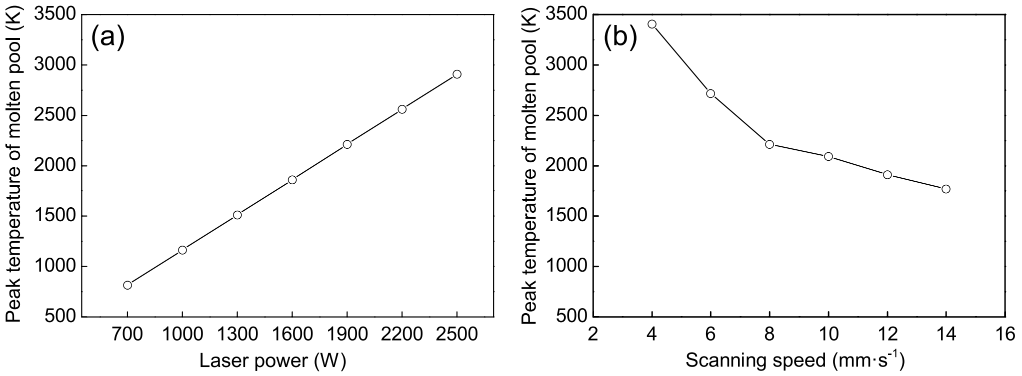

Fig. 24: Changes in peak temperature of molten pool on changing process parameters of laser power (a), and scanning speed (b)

Incompletely melted powder leads to the formation of lack-of-fusion pores defects, which also results in an increase in the surface roughness.

5 Conclusions

The changes of formability, microstructure, and micro-hardness of the novel LAM Ti-6.38Al-3.87V-2.43Mo alloy single-track and bulk samples with different processing parameters were investigated in this work. The major conclusions are as follows:

(1) The surface roughness can be controlled by varying the LAM processing parameters, including the laser power and scanning speed. Under a laser power of 1,900 W at a scanning speed of 8 mm·s^{-1}, the single-track layer exhibits minimal surface roughness and good formability.

(2) Laser power plays a significant role in determining the relative density of the LAM bulk samples. Under a laser power of <1,600 W, there is an apparent lack-of-fusion defects that reduce the density of the samples. However, at a laser power of 1,900 W, there is no apparent decrease in the density with the change in the scanning speed.

(3) The microstructure of the novel LAM Ti-6.38Al-3.87V-2.43Mo alloy is influenced by the laser power and scanning speed. With an increased laser power or a decreased scanning speed, the input energy is greater to reduce the cooling rate, resulting in a coarsening of the microstructure that reduces the micro-hardness of the alloy.

Acknowledgements

This work was supported by the National Key Research and Development Program of China (No. 2016YFB1100103), and the Key Discipline and Major Project of Dalian Science and Technology Innovation Foundation (No. 2020JJ25CY004).

References

[1] Banerjee D, Williams J C. Perspectives on titanium science and technology. Acta Mater., 2013, 61(3): 844–879.
[2] Roger R R. An overview on the use of titanium in the aerospace industry. Mater. Sci. Eng. A, 1996, 213: 103–114.
[3] Liu T Y, Liu H Y, Yao Q, et al. Microstructure and mechanical properties of laser additive manufactured novel titanium alloy after heat treatment. China Foundry, 2021, 18(6): 574–580.
[4] Liu T Y, Zhu Z H, Zhang S, et al. Design for Ti-Al-V-Mo-Nb alloys for laser additive manufacturing based on a cluster model and on their microstructure and properties. China Foundry, 2021, 18(4): 424–432.
[5] Azarniya A, Colera X G, Mirzaali M J, et al. Additive manufacturing of Ti-6Al-4V parts through laser metal deposition (LMD): Process, microstructure, and mechanical properties. J. Alloy. Compd., 2019, 804: 163–191.
[6] Zhu Y Y, Tian X J, Li J, et al. Microstructure evolution and layer bands of laser melting deposition Ti-6.5Al-3.5Mo-1.5Zr-0.3Si titanium alloy. J. Alloy. Compd., 2014, 616: 468–474.
[7] Zhang D Y, Qiu D, Gibson M A, et al. Additive manufacturing of ultrafine-grained high-strength titanium alloys. Nature, 2019, 576(7785): 91–95.
[8] Yu Q, Wang C S, Wang D, et al. Microstructure and properties of Ti-Zr congruent alloy fabricated by laser additive manufacturing. J. Alloy. Compd., 2020, 834: 155087.
[9] Dong C, Wang Z J, Zhang S, et al. Review of structural models for the compositional interpretation of metallic glasses. Int. Mater. Rev., 2019, 65(5): 286–296.
[10] Dong C, Dong D D, Wang Q. Chemical units in solid solutions and alloy composition design. Acta. Metall. Sin., 2018, 54: 293–300.
[11] Dong C, Wang Q, Qiang J B, et al. From clusters to phase diagrams: Composition rules of quasicrystals and bulk metallic glasses. J. Phys. D. Appl. Phys., 2007, 40: R273–R291.
[12] Takeuchi A, Inoue A. Classification of bulk metallic glasses by atomic size difference, heat of mixing and period of constituent elements and its application to characterization of the main alloying element. Mater. Trans., 2005, 46: 2817–2829.
[13] Zhang J, Wang Q, Wang Y M, et al. Effect of heat treatment on the highly corrosion-resistant Cu70Ni27.7Fe2.3 alloy. J. Alloy. Compd., 2010, 505(2): 505–509.
[14] Wang Z R, Qiang J B, Wang Y M, et al. Composition design procedures of Ti-based bulk metallic glasses using the cluster-plus-glue-atom model. Acta Mater., 2016, 111: 366–376.
[15] Jiang B B, Wang Q, Wen D H, et al. Effects of Nb and Zr on structural stabilities of Ti-Mo-Sn-based alloys with low modulus. Mater. Sci. Eng. A, 2017, 687: 1–7.
[16] Wu X H, Liang J, Mei J F, et al. Microstructures of laser-deposited Ti-6Al-4V. Mater. Des., 2004, 25: 137–144.
[17] Yang J J, Han J, Yu H C, et al. Role of molten pool mode on formability, microstructure and mechanical properties of selective laser melted Ti-6Al-4V alloy. Mater. Des., 2016, 110: 558–570.
[18] Thijs L, Verhaeghe F, Craeghs T, et al. A study of the microstructural evolution during selective laser melting of Ti-6Al-4V. Acta Mater., 2010, 58(9): 3303–3312.
[19] Ohnuma I, Enoki H, Ikeda O, et al. Phase equilibria in the Fe-Co binary system. Acta Mater., 2002, 50(2): 379–393.
[20] Enkhtor L, Galbadrakh R, Silonov V. Short-range order and static displacements in polycrystalline Ni-13.1at.%W alloy. Solid. State. Phenom., 2018, 271: 98–105.
[21] Villars P, Calvert L D. Pearson's handbook of crystallographic data for intermetallic phases. ASM International, 1985.
[22] Jiang B B, Wang Q, Dong C, et al. Exploration of phase structure evolution induced by alloying elements in Ti alloys via a chemical-short-order cluster model. Sci. Rep., 2019, 9: 3404.
[23] Dong D D, Zhang S, Wang Z J, et al. Composition interpretation of binary bulk metallic glasses via principal cluster definition. Mater. Des., 2016, 96: 115–121.
[24] Qian S N, Dong C, Liu T Y, et al. Solute-homogenization model and its experimental verification in Mg-Gd-based alloys. J. Mater. Sci. Technol., 2018, 34: 1132–1141.
[25] Wu H, Zhao Y, Ge P, et al. Effect of β stabilizing elements on the strengthening behavior of titanium α phase. Rare Met. Mater. Eng., 2012, 41(5): 805–810.
[26] Ren Y M, Lin X, Fu X, et al. Microstructure and deformation behavior of Ti-6Al-4V alloy by high-power laser solid forming. Acta Mater., 2017, 132: 82–95.
[27] Bäuerle D. Laser processing and chemistry. Springer, Berlin/New York, 2011.
[28] Mills K C. Recommended values of thermophysical properties for selected commercial alloys. Cambridge, 2002.
[29] Rubenchik A, Wu S, Mitchell S, et al. Direct measurements of temperature-dependent laser absorptivity of metal powders. Appl. Opt., 2015, 54: 7230–7233.